

CIRP Conference on Electro Physical and Chemical Engineering

Numerical analysis of the impact of the ECM inlet geometry on the electrolyte flow and its interaction with a thin-walled workpiece

Daniel Lauwers^{a,*}, Elio Tchoupe Sambou^b, Tim Herrig^b, Matthias Meinke^{a,c}, Andreas Klink^b, Dominik Krug^a, Wolfgang Schröder^{a,c}^aChair of Fluid Mechanics and Institute of Aerodynamics (AIA), RWTH Aachen University, Willnerstr. 5a, 52062 Aachen, Germany^bManufacturing Technology Institute – MTI of RWTH Aachen University, Campus-Boulevard 30, Aachen 52074, Germany^cJARA Center for Simulation and Data Science, RWTH Aachen University, Seffenter Weg 23, 52074 Aachen, Germany* Corresponding author. Tel.: +49 241 80 91962. E-mail address: d.lauwers@aia.rwth-aachen.de

Abstract

The numerical simulation of the (precise) electrochemical machining (P)ECM process faces many challenges due to the interaction of the various physical effects involved, the wide range of spatial and temporal time scales, and the limited experimental access to the process for the validation of numerical methods. The material removal in the working gap is largely determined by the electrical field and the multiphase flow of the electrolyte. Due to limited optical access into the working gap, not much is known about the details. However, an accurate numerical simulation of the machining process needs information about gas bubble sizes, local bubble concentration and the fluid structure interaction. This paper presents advanced simulations of electrolyte flow in the ECM process applied to thin-walled turbomachinery blades, incorporating process gas transport. To the best of the authors' knowledge, turbulent electrolyte flow is predicted using a large-eddy simulation (LES) approach for the first time in ECM research. To address the high computational cost of LES, two reduced model configurations are also evaluated. The results are compared in terms of the electrolyte flow field, the transport of the process gases, and the forces that the electrolyte exerts on the workpiece. The results reveal that the conditions upstream of the working gap have a non-negligible influence on the flow field in the gap and have to be carefully chosen depending on the focus of the simulations. Furthermore, the simulation effort could be reduced by 16% and 31% using shortened inlet configurations, which were still able to reproduce most of the physical effects captured in the full simulation.

© 2025 The Authors. Published by Elsevier B.V.

This is an open access article under the CC BY-NC-ND license (<https://creativecommons.org/licenses/by-nc-nd/4.0>)

Peer review under the responsibility of the scientific committee of the ISEM2025 Conference

Keywords: ECM; large-eddy simulation; HPC; fluid mechanics; multiphase flow

1. Introduction

The electrochemical machining (ECM) process for bulk material removal and the precise ECM (PECM) process for surface finishing represent complex multiphysical systems that are influenced by the various parameters defining the operating conditions, the geometry and material of the workpiece, etc.. The current density distribution in the working gap that drives the material removal is affected by the temperature distribution and process gas concentration in the electrolyte and the deflection of the workpiece geometry due to the fluid-structure interaction (FSI). This makes the determination of optimal machining parameters and tool geometries for an efficient process with high manufacturing accuracy difficult. Presently, this process design is often done iteratively and parameters are chosen conservatively to prevent shape deviations in the finished work-

piece or even catastrophic short-circuit events caused by excessive workpiece deflection. To facilitate tool design and parameter optimization, numerical models of the (P)ECM process that can predict the cathode geometry, workpiece deflection and corresponding shape deviations need to be developed.

Such multiphysics numerical models, with varying complexity and coupling approaches, have been proposed. For example, in [1] and [2] the transient electric field and associated material removal have been modeled without an explicit modeling of the electrolyte flow. Homogenized models have been used for the anodic dissolution of moving cathodes [3, 4]. Studies that include electrolyte flow, e.g. [5, 6], generally employ the Reynolds-Averaged Navier-Stokes (RANS) equations that only provide approximate time-averaged solutions of turbulent flows. In [6], the RANS model was unidirectionally coupled to a 2D structural mechanics solver for the workpiece deflection. While these simplified models can serve as a starting point,

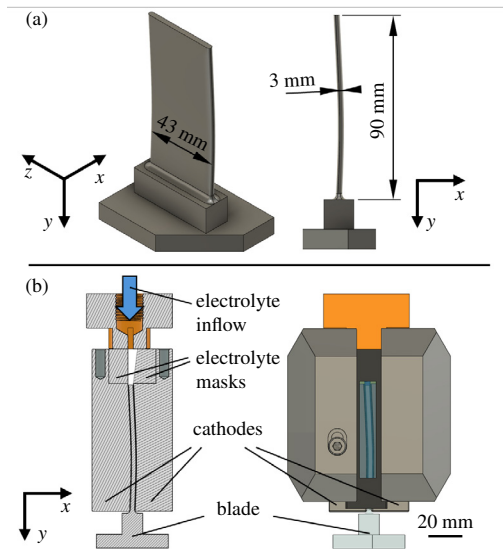


Fig. 1. (a) Dimensions of the blade geometry. (b) Components of the (P)ECM machining setup, depicted in a cut view (left) and with the surrounding machine components (right).

they do not fully capture the intricate, time-dependent behavior and three-dimensional effects. To address these limitations, advanced models using large-eddy simulation (LES) can provide a more accurate representation of transient, three-dimensional flow dynamics. LESs explicitly resolve large parts of the turbulent spectrum, thereby offering detailed insights into electrolyte flow, gas transport, and their impact on workpiece deflection, leading to better predictions for complex geometries. Especially flows around sharp edges, that are often found in inlet geometries upstream of the working gap or at the tip of turbine blades, cannot be accurately predicted with RANS approaches.

To provide reference or validation data for the verification of the accuracy of a simulation method, an experimental setup was developed in [7]. It provides optical access to the working gap that enables the time-resolved measurement of the workpiece deflection. In this paper, results from electrolyte flow simulations of this setup are discussed. The focus is on the influence of the inlet geometry on the conditions in the working gap. In general, the inlet geometry has an influence on the flow conditions in the working gap, up to the point at which the state of a fully developed channel flow is reached. However, since the volume of the inlet geometry represents a significant fraction of the total volume including the working gap, shortening the numerical domain upstream of the working gap can significantly reduce simulation time and computational resources.

2. ECM setup

A (P)ECM setup for the manufacturing of high pressure compressors for turbomachinery is considered. These blades are usually thin for aerodynamic reasons and are only supported at the base of the blade. The (P)ECM processing for these blades is performed from both sides with cathodes surrounding the workpiece. The multiphase electrolyte flow in the (P)ECM setup presented in [7] is simulated. While the setup

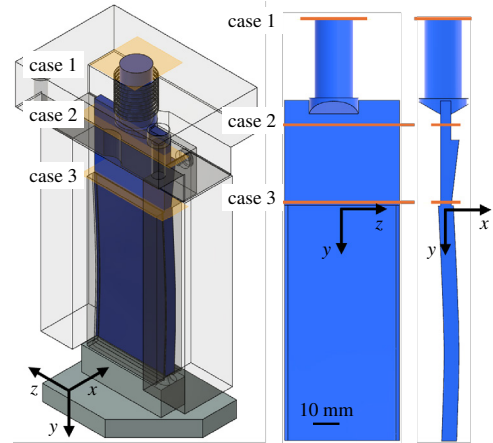


Fig. 2. The simulation domain of the electrolyte flow with the three inflow planes for cases 1 to 3. The surrounding components of the tool assembly are shown transparent.

supports the transient PECM conditions, no mechanical oscillation or pulsed currents are considered. Although the setup incorporates custom optical access to the working gap, the electrolyte flow follows the typical path from the blade tip to its base used for the manufacturing of such components. The geometry of the workpiece and the machining fixture including cathodes and the electrolyte mask are shown in figure 1. The size of the working gap is 0.5 mm.

The electrolyte flow in the ECM setup is simulated for three configuration, i.e., a baseline configuration and two reduced configurations. They differ in the position of the inlet plane. The electrolyte is delivered to the machining setup through a hose. Case 1 represents the baseline configuration, where the computational domain includes part of this hose. In case 2, the first part of the inlet geometry, where the cross-section changes from circular to rectangular, is omitted in the simulation, but the remaining part of the inlet geometry, including the flow past the electrolyte masks, is kept. The electrolyte masks are designed to bridge the gap between inlet and working gap for a wide range of blade thicknesses and gap heights. Case 3 represents the shortest simulation domain that starts only 2 mm upstream of the blade tip. The locations of the different inflow planes are shown in figure 2.

An electrolyte flow rate f of 371 min^{-1} ($6.173 \cdot 10^{-4} \text{ m}^3 \text{ s}^{-1}$) is prescribed for the setup with the Reynolds number

$$Re = \frac{u_B H}{\nu_l} = 5865, \quad (1)$$

where u_B is the bulk velocity, H the height of the working gap, and ν_l the kinematic viscosity of the electrolyte. These operating conditions agree with an electrolyte pressure drop of 1 bar over the working gap, when a turbulent flow is assumed [7]. Given the significant computational cost of LES, an atypical current density of 0.044 A mm^{-2} is assumed as a starting point. This choice results in a reduced gas production rate, which can be derived from Faraday's law

$$\dot{m}_g = I \frac{M}{z F}, \quad (2)$$

where \dot{m}_g is the gas production rate, I the electrical current, M the molar mass, z the chemical valence, and F Faraday's constant. For a current efficiency of 100% this results in a gas production rate of $1.38 \cdot 10^{-4} \text{ kg s}^{-1}$ which corresponds to a gas volume fraction of approximately 5% at the end of the working gap. Additionally, it is assumed that the gas is pure hydrogen that forms at the cathodes, as the proportion of oxygen that forms on the workpiece is small in comparison.

3. Numerical methods

3.1. Electrolyte flow CFD model

The simulations were performed with the open source multiphysics simulation framework m-AIA [8] that contains multiple numerical solvers for the large-scale simulation of multiphysical problems [9, 10, 11]. The electrolyte flow is modeled using the lattice Boltzmann (LB) solver of m-AIA. Instead of directly solving the macroscopic conservation equations for fluids, i.e. the Navier-Stokes equations, the LB method solves the discrete-velocity Boltzmann equation. It can be shown that the discretized Boltzmann equation mathematically converges to the Navier-Stokes equations for low Mach numbers, i.e., for weakly compressible flows [12]. The LB algorithm consists of two simple operations, namely the collision step, which is a local operation in each mesh cell, and the streaming step, which propagates information to neighbouring cells. Therefore, the LB method can be easily implemented on massively parallel computers, i.e., high-performance computing (HPC) hardware, and becomes computationally more efficient than classical Navier-Stokes solvers such as the finite-volume method. A cumulant-based collision step is used as part of the LB method, since it has better stability properties for fully turbulent, high Reynolds number flows [13]. Turbulence scale resolving LES are performed, where the smallest turbulent scales are modeled using a Smagorinsky-type subgrid scale model.

3.2. Gas transport model

The gas transport in the electrolyte flow is predicted using a Lagrangian particle tracking method. In this approach, the individual gas bubbles are represented as point particles in a Lagrangian frame of reference and interact with the liquid flow through momentum-exchange terms [14]. The Newtonian motion equations are formulated as

$$\frac{\partial \mathbf{x}_b}{\partial t} = \mathbf{u}_b, \quad \rho_b V_b \frac{\partial \mathbf{u}_b}{\partial t} = \mathbf{F}_b. \quad (3)$$

For each bubble, \mathbf{x}_b is the position, \mathbf{u}_b the velocity, ρ_b the density, V_b the volume, and \mathbf{F}_b the force acting upon the bubble by the liquid phase. The force acting on each bubble consists of the drag force \mathbf{F}_D , the force due to stress gradients \mathbf{F}_S , the lift force \mathbf{F}_L , and the added mass force \mathbf{F}_A . The individual terms are

$$\mathbf{F}_b = \mathbf{F}_D + \mathbf{F}_S + \mathbf{F}_L + \mathbf{F}_A \quad (4)$$

$$\mathbf{F}_D = -\frac{1}{2} C_D \rho_l \pi r_b^2 |\mathbf{u}_b - \mathbf{u}_l| (\mathbf{u}_b - \mathbf{u}_l) \quad (5)$$

$$\mathbf{F}_S = \rho_l V_b \frac{\partial \mathbf{u}_l}{\partial t} \quad (6)$$

$$\mathbf{F}_L = -C_L \rho_l V_b (\mathbf{u}_b - \mathbf{u}_l) \times \nabla \times \mathbf{u}_l \quad (7)$$

$$\mathbf{F}_A = -C_A \rho_l V_b \left(\frac{\partial \mathbf{u}_b}{\partial t} - \frac{\partial \mathbf{u}_l}{\partial t} \right), \quad (8)$$

where C_D , C_L , and C_A are the coefficients of drag, lift and added mass, ρ_l and \mathbf{u}_l are the liquid density and velocity at the bubble position, and r_b is the bubble radius. A Stokes drag force model is used for the determination of the drag coefficient C_D

$$C_D = \frac{24}{Re_b}, \quad Re_b = \frac{|\mathbf{u}_b - \mathbf{u}_l| 2r_b}{\nu_l}, \quad (9)$$

where Re_b is the slip Reynolds number and ν_l is the kinematic viscosity of the liquid phase [15]. For the added mass and lift forces, the coefficients are assumed to be $C_A = 0.5$ and C_L as a function of the Reynolds number Re_b and the fluid properties following [16]. Buoyancy forces are omitted, since they are negligible compared to the other forces in the present setup with an assumed bubble diameter of $2.5 \cdot 10^{-5} \text{ m}$. The bubble size also motivates the usage of the models for non-deformable, spherical bubbles. In the real process, the gas bubbles nucleate at the cathode surface and grow until a critical size is reached and the forces of the fluid are sufficiently large to separate them from the wall. In the numerical model, the nucleation phase is omitted since the focus lies on the transport of the process gas by the electrolyte. As such, the bubbles are spawned at the wall with their final size. Coalescence is also neglected in the model.

3.3. Computational grid and boundary conditions

The LB method of m-AIA uses an unstructured Cartesian grid with local refinement. Various refinement methods are available within m-AIA. For the present work, a uniform background mesh with a cell length of $3.955 \cdot 10^{-5} \text{ m}$ is used and a static mesh refinement is chosen, where all inlet walls and the entire working gap are refined by one level, which cuts the cell length in half. The computational grid for the three inlet configurations is identical downstream of the inflow plane, ensuring that any variations in the results are due to differences in the inlet configuration. The cell length of the finer grid level is chosen as $1.978 \cdot 10^{-5} \text{ m}$. For the Mach number 0.1 chosen in the LB method, this results in a time step size of $9.733 \cdot 10^{-8} \text{ s}$. A slice of the computational grid at the inflow of the working gap with the location and orientation of the coordinate system at the center of the blade tip is shown in figure 3. For the complete inlet setup, i.e. case 1, the total number of cells amounts to 1.2 billion. This number is reduced to 1.0 billion cells for case 2 and 0.81 billion cells for case 3. The grid is stored in a hierarchical tree data structure and partitioned for parallel execution according to a space-filling Hilbert curve. The simulations are performed on the *Hawk* HPC system, installed at the High Performance Computing Center (HLRS) in Stuttgart, Germany. Each simulation was performed on 128 compute nodes with 128 CPU cores each, resulting in a total number of 16,384 parallel CPU cores. The number of particles representing the gas bubbles is on the order of 10 million.

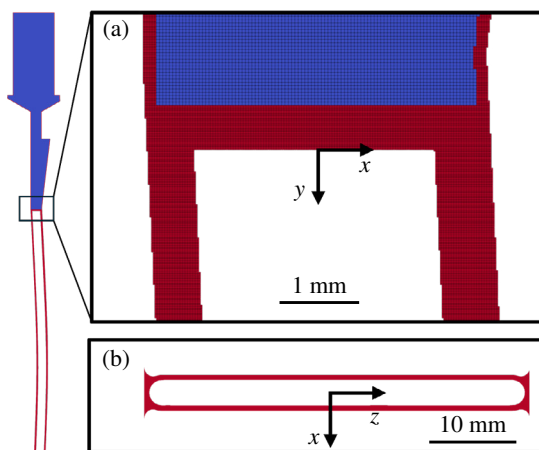


Fig. 3. (a) $x-y$ -Slice of the Cartesian grid with grid refinement around the blade tip and (b) $x-z$ -slice of the grid showing the cross-section of the working gap. The finer grid level is shown in red, the coarser level is shown in blue. The origin of the coordinate system is located at the center of the blade tip.

No-slip boundary conditions for the LB method are typically realized with bounce-back boundary conditions. They work by inverting those discrete velocity distribution components that intersect the wall. An interpolated bounce-back condition is applied to all walls that supports bounce-back at arbitrary wall positions between cell centers to model the complex geometry fluid domain [17]. The momentum exchange, i.e., the force enacted by the fluid on the wall can be directly calculated by summation of the inverted velocity distributions. For the outflow, a non-reflecting pressure boundary condition similar to the outflow condition by Finck et al. [18] is used. At the inflow, a halfway bounce-back condition with a prescribed velocity distribution is used. To model turbulent inflow conditions at the specific Reynolds number of the flow, the prescribed mean velocity profiles are superimposed with turbulent fluctuations. The fluctuations are generated according to the conditions in a fully developed turbulent pipe flow (case 1) or rectangular duct flow (case 2 and 3). The bulk flow rate is identical for all cases.

As an initial condition for the simulations, a quiescent flow state without any process gas is prescribed. The inflow velocity is ramped from zero to its steady value over 40,000 time steps to prevent any pressure spikes. Once the electrolyte flow has reached a statistically steady state after approximately 400,000 time steps, the gas production is started. The bubbles representing the process gas are spawned with a uniform distribution on the surface of the cathodes and with a constant mass flow rate.

4. Results

4.1. Electrolyte flow field

For the chosen Reynolds numbers, a fully turbulent flow field develops throughout the inlet geometry and the working gap for all cases. The instantaneous velocity field for case 1 is shown in figure 4. Flow separation and recirculation zones can be observed at various regions with sharp edges. Downstream of the blade tip, the flow state quickly approaches that of a turbulent

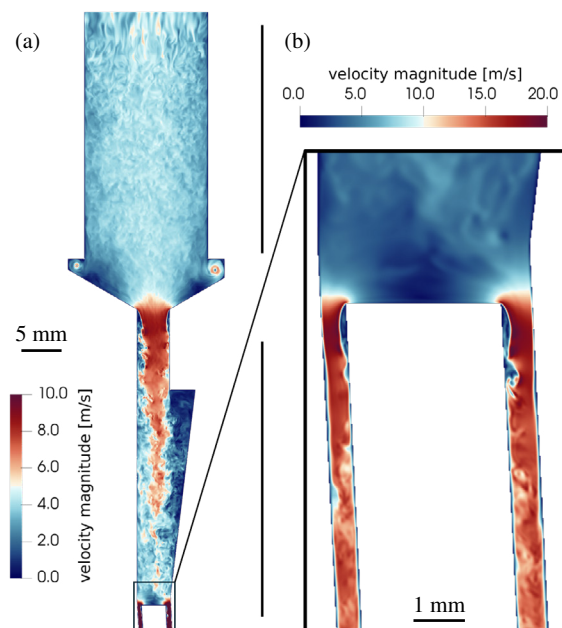


Fig. 4. Instantaneous velocity field for case 1 on a slice through the centerline of the inlet pipe. In (a) the region of the inlet is shown, in (b) the flow around the tip of the blade is shown.

channel flow. Due to the curvature of the blade, the velocity profile retains a slight asymmetry. In figure 5, the mean velocity in y -direction v and the turbulence kinetic energy (TKE) k are plotted for the left and right working gap at the blade centerline, 10 mm downstream of the blade tip. The local coordinates x'_l and x'_r start at the respective gap wall. The TKE is a measure for the kinetic energy of the turbulent scales in the flow. It is calculated from the mean square of the velocity components

$$k = \frac{1}{2} \left(\overline{(u')^2} + \overline{(v')^2} + \overline{(w')^2} \right), \quad (10)$$

where the fluctuating velocities u' , v' , w' (in x , y , and z direction) are determined as the deviations of the respective instantaneous velocities from their temporal mean, e.g. $u' = u - \bar{u}$. The mean velocity profiles for cases 1 and 2 agree very well with an average deviation of 1.3%, while a slightly larger deviation is observed for case 3 with an average deviation of 4.9%. Regarding the TKE, cases 1 and 3 show a slightly better agreement than case 1 and 2, but with an average deviation of 5.1% and 13.2% all cases capture the turbulent character of the flow equally well.

4.2. Gas transport

In the simulations, a constant-rate, uniformly distributed gas production is assumed. This leads to a statistically steady distribution of bubbles throughout the working gap where the gas concentration increases with the distance from the blade tip y . In figure 6, the instantaneous bubble distribution throughout the working gap for case 1 and a comparison of the bubble distribution at the center of the blade tip for all three cases is shown. The distributions for cases 1 and 2 look nearly identical. For case 3, the velocities of the bubbles are slightly higher com-

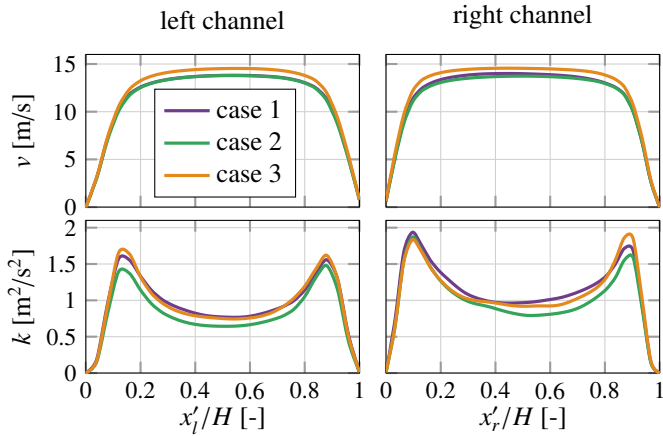


Fig. 5. The mean y-component of the velocity v and turbulence kinetic energy (TKE) k in the left and right working gap plotted at the centerline of the blade at $y = 10$ mm.

pared to the other cases, which is consistent with the slightly higher electrolyte velocity in the gap center shown in figure 5. Additionally, a slightly large number of bubbles can be observed in the recirculation region near the blade tip for case 3.

For the quantitative analysis of the gas distribution within the working gap, the bubble distribution density g has been calculated along the y- and z-axes, which represents the number of bubbles per length unit. The distribution density g_y along the y-axis plotted in figure 7(a) shows a linear growth. Additionally, the accumulation of some bubbles in the recirculation region, which is stronger for case 3 than for the other two cases, is visible. Downstream of the recirculation region, the slope of g_y is slightly lower for case 3 compared to the other cases, which is consistent with the higher bubble velocity. When analyzing the distribution density along the z-axis (g_z) as shown in figure 7(b), case 3 exhibits an approximately 8% lower density in the central 10 mm of the blade compared to the other cases, which show nearly identical distributions. On the other hand, the density near the blade edges is higher for case 3. The drop in density for all cases in this region can be attributed to the improved gas transport due to the larger flow cross-section at the edges of the machining setup (cf. figure 3(b)).

4.3. Workpiece forces

Due to the curvature of the blade, the machining setup is not symmetric. This leads to different pressures exerted from the electrolyte on the two sides of the workpiece. Additionally, the turbulent nature of the flow adds fluctuating force components to a steady net force. The quantitative analysis of the force acting on the workpiece is important for the determination of the process parameters, since it causes a deflection of the workpiece. This can lead to shape deviations and, in extreme cases, even cause short circuits between the cathode and anode. The x-component of the net force acting on the workpiece is plotted over time in figure 8(a). Cases 2 and 3 exhibit a relatively steady behavior, with a mean of -10.6 N and -11.6 N average net force. Case 1 has a slightly lower absolute force with a mean of -9.6 N but higher fluctuations. To put these forces into context, the

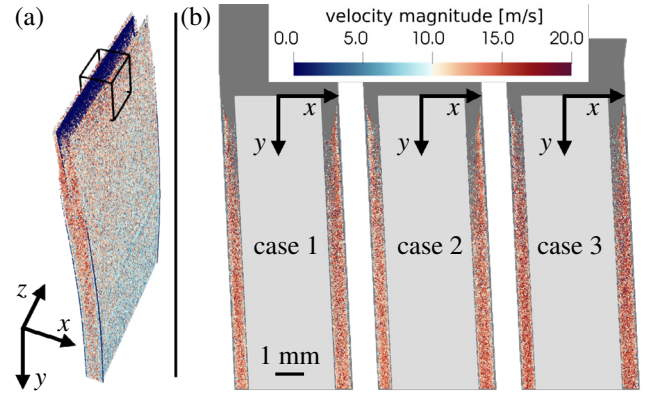


Fig. 6. (a) Snapshot of the bubble distribution in the working gap for case 1, colored by the velocity magnitude $|u_b|$. (b) Snapshot of the gas distribution for the three cases at the center of the blade tip (region marked in (a)), colored by the velocity magnitude.

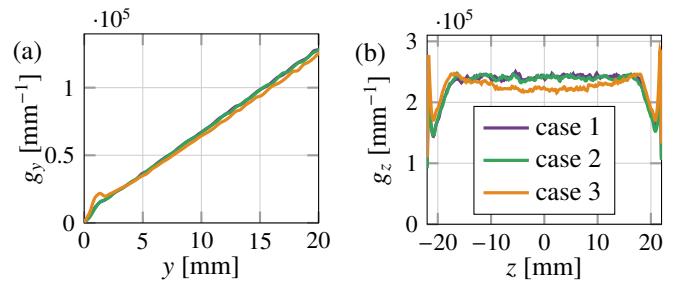


Fig. 7. Bubble distribution density g plotted over the y-axis near the blade tip (a) and over the z-axis for the whole working gap (b).

static deflection of the workpiece tip reaches 0.050 mm (case 1), 0.055 mm (case 2), and 0.045 mm (case 3) when applying these mean forces to the workpiece. For a gap height of 0.5 mm, this represents a significant change in the geometry of the working gap. The spectral distributions of the fluctuation amplitudes were determined for the three cases with a fast Fourier transform (FFT) and are plotted in figure 8(b) as a function of the frequency. Higher fluctuations at low frequencies are apparent for case 1. These low frequency fluctuations are especially relevant for the present case, since the lowest eigenfrequency of the 3 mm blade geometry was 273 Hz in [7]. Apart from the low frequencies, the fluctuations have a peak at 1400 Hz for all cases, but the amplitude is higher for case 1.

5. Conclusion and Outlook

A numerical method for the simulation of the electrolyte flow, gas transport, and forces exerted by the electrolyte on the workpiece in the ECM process is presented. The LES method used in this work is coupled to a Lagrangian particle tracking approach that models the transport of the process gas within the electrolyte. To the authors' knowledge, this study marks the first application of an LES method in this field. As a starting point, an atypical current density was used to keep the gas flow rate low. Three configurations were considered, that differ in the length of the inlet geometry resolved in the simulation domain upstream of the working gap. The shorter configurations

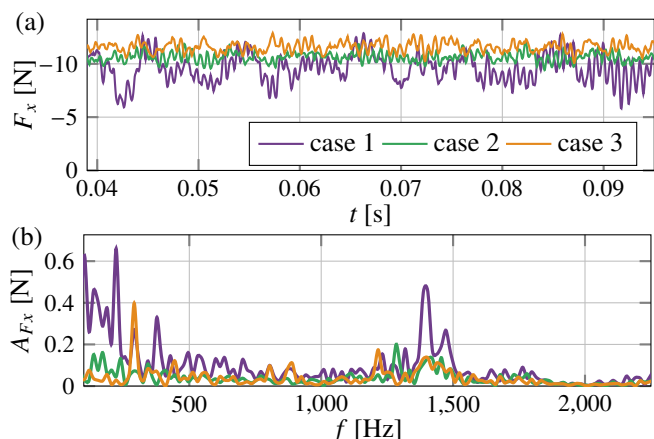


Fig. 8. (a) x -component of the resulting force on the workpiece F_x plotted over time, (b) amplitude spectrum of F_x plotted over the frequency.

result in a reduction of the computational effort between 16% and 31%. The simulation results are characterized regarding the liquid flow field, the gas transport, and the forces acting on the thin-walled workpiece.

All three configurations show similar results for the turbulent flow field, with mean velocities differing by an average of less than 5% and the turbulent kinetic energy by less than 15%. The two cases with the longer inlet geometry produce almost identical results regarding the gas transport, with the third case resulting in a prediction of the bubble distribution that differs by about 8%. In the analysis of the forces acting on the workpiece, the largest differences between the configurations are found. The predicted average forces differ by 18% in the three setups, additionally differences in the fluctuating behavior of the forces exist. The two shorter configurations, cases 2 and 3 produce fluctuations at lower amplitude than the setup with the longest configuration, i.e., case 1. In summary, all configurations capture the general behavior of the ECM process well, but especially when precise predictions of gas transport or workpiece forces are required, computations domains resolving the full inlet geometry seem to be necessary.

These results are the basis for further simulations of the (P)ECM process with higher current densities. They enable the selection of appropriate domain boundaries for the numerical simulations to achieve accurate prediction of the physical quantities of interest. In a next step, the gas transport in the process will be further analyzed focussing on the prediction of shape deviations due to the change of the electrolyte properties. This can be achieved by using the time-resolved information about the gas concentration from the present method to determine the local material removal rate. Another area of interest is the fluid-structure interaction (FSI) of thin-walled workpieces with the electrolyte that not only can lead to geometric deviations, but even catastrophic short-circuit events that damage the workpiece and tool.

Acknowledgements

The German Research Society (DFG) provided financial support for the research presented in this paper within the Priority Program SPP2231-FLUSIMPRO *Simulation of the pulsed*

electrochemical machining (PECM) of thin-walled workpieces for turbomachinery component manufacture – SIMPECT.

The Gauss Centre for Supercomputing provided HPC access for the numerical simulations presented in this paper through a GCS Large-Scale project.

References

- [1] F. Boettcher, I. Schaarschmidt, J. Edelmann, A. Schubert, Simulation-assisted tool design for pulsed electrochemical machining of magnetic shape-memory alloys, *J. manuf. mater. process.* (03 2024). doi:10.3390/jmmp8020046.
- [2] A. Zhang, Z. Xu, L. Jiangwei, Y. Wang, Improvement of blade platform accuracy in ECM utilizing an auxiliary electrode, *Mater. Manuf. Process.* 35 (2020) 951–960. doi:10.1080/10426914.2020.1752920.
- [3] T. van der Velden, B. Rommes, A. Klink, S. Reese, J. Waimann, A novel approach for the efficient modeling of material dissolution in electrochemical machining, *Int. J. Solids Struct.* 229 (2021) 111106. doi:10.1016/j.ijsolstr.2021.111106.
- [4] A. Schmidt, T. van der Velden, S. L. T. Ritzert, S. Reese, J. Waimann, A homogenized description for electrochemically induced material dissolution, in: *Proc. of the 20th INSECT 2024*, Aachen, Germany, 2024, pp. 83–91. doi:10.18154/RWTH-2024-10238.
- [5] M. Aslan, B. Kanber, H. Demirtas, B. Sungur, Investigation of electrolyte pressure effect on blisk blades during electrochemical machining, *Multidiscip. Model. Mater. Struct.* 20 (2024) 448–465. doi:10.1108/MMMS-08-2023-0270.
- [6] E. Tchoupe Sambou, T. Petersen, A. Klink, T. Herrig, T. Bergs, Simulation-based investigation of flushing-induced workpiece deflection in electrochemical machining, in: *Proc. of the 20th INSECT 2024*, Aachen, Germany, 2024, pp. 93–100. doi:10.18154/RWTH-2024-10239.
- [7] E. Tchoupe Sambou, D. Lauwers, T. Petersen, T. Herrig, A. Klink, M. Meinke, W. Schröder, Investigating workpiece deflection in precise electrochemical machining of turbine blades, *J. manuf. mater. process.* 8 (4) (2024). doi:10.3390/jmmp8040138.
- [8] Institute of Aerodynamics, m-AIA (Aug. 2024). URL <https://git.rwth-aachen.de/aia/m-AIA/m-AIA>
- [9] L. Schneiders, M. Meinke, W. Schröder, Direct particle–fluid simulation of Kolmogorov-length-scale size particles in decaying isotropic turbulence, *J. Fluid Mech.* 819 (2017) 188–227. doi:10.1017/jfm.2017.171.
- [10] D. Hartmann, M. Meinke, W. Schröder, The constrained reinitialization equation for level set methods, *J. Comput. Phys.* 229 (5) (2010) 1514–1535. doi:10.1016/j.jcp.2009.10.042.
- [11] S. Herff, K. Pausch, S. Loosen, W. Schröder, Impact of non-symmetric confinement on the flame dynamics of a lean-premixed swirl flame, *Combust. Flame* 235 (2022). doi:10.1016/j.combustflame.2021.111701.
- [12] T. Krüger, H. Kusumaatmaja, A. Kuzmin, O. Shardt, G. Silva, E. M. Viggen, *The Lattice Boltzmann Method - Principles and Practice*, Springer International, 2016. doi:10.1007/978-3-319-44649-3.
- [13] M. Geier, M. Schönherr, A. Pasquali, M. Krafczyk, The cumulant lattice Boltzmann equation in three dimensions: Theory and validation, *Comput. Math. Appl.* 70 (2015) 507–547. doi:10.1016/j.camwa.2015.05.001.
- [14] R. Sungkorn, J. Derksen, J. Khinast, Modeling of turbulent gas–liquid bubbly flows using stochastic lagrangian model and lattice-Boltzmann scheme, *Chem. Eng. Sci.* 66 (12) (2011). doi:10.1016/j.ces.2011.03.032.
- [15] A. Tomiyama, I. Kataoka, I. Zun, T. Sakaguchi, Drag coefficients of single bubbles under normal and micro gravity conditions, *JSME Int. J. Ser. B* 41 (2) (1998) 472–479. doi:10.1299/jsmeb.41.472.
- [16] A. Tomiyama, H. Tamai, I. Zun, S. Hosokawa, Transverse migration of single bubbles in simple shear flows, *Chem. Eng. Sci.* 57 (11) (2002) 1849–1858. doi:10.1016/S0009-2509(02)00085-4.
- [17] M. Bouzidi, M. Firdaouss, P. Lallemand, Momentum transfer of a Boltzmann-lattice fluid with boundaries, *Phys. Fluids* 13 (11) (2001) 3452–3459. doi:10.1063/1.1399290.
- [18] M. Finck, D. Hänel, I. Wlokas, Simulation of nasal flow by lattice Boltzmann methods, *Comput. Biol. Med.* 37 (6) (2007) 739–749. doi:10.1016/j.combiomed.2006.06.013.